Chapter 2 The Mean Meridional Circulation of the Martian Atmosphere

2.1 Introduction

During some martian dust storms, atmospheric temperatures at ~15—35 km above the winter (always northern) pole warm dramatically over the course of a few martian days by up to 80 K [*Jakosky and Martin*, 1987]. While some of the warming equatorward of ~65º S can be explained by direct solar heating of dust advected from the southern hemisphere or the northern tropics, the warming within polar night ("dust storm polar warming") cannot be due to the absorption of solar radiation. Instead, dust storm polar warming is likely due to adiabatic heating from strong downwelling over the pole, in particular downwelling of the principal meridional overturning cell (PMOC), sometimes called, "the Hadley cell," which may be especially intense during strong dust storms [*Haberle et al.*, 1982; *Schneider*, 1983; *Haberle et al.*, 1993].

When the first wave-resolving, three-dimensional model of the martian general circulation was developed in the early 1990s [*Haberle et al.*, 1993], it could not simulate dust storm polar warmings, since the downwelling of the simulated PMOC never penetrated further than 65º—70º N, which *Haberle et al.* [1993] attributed to insufficiently strong eddy transport of heat and momentum. *Wilson* [1997] successfully simulated a dust storm polar warming by using a deeper vertical domain than used by *Haberle et al.* [1993] and resolving the atmospheric thermal tides. The deep vertical domain both reduced the sensitivity of the simulation to dissipation at the model top and also improved how the PMOC (and the thermal tides) during the dust storm were resolved vertically. The atmospheric thermal tides transported sufficient easterly angular momentum to drive the PMOC downwelling closer to the north pole. Simulations of the polar warming by *Forget et al.* [1999] and *Kuroda et al.* [2009] have been successful for similar reasons.

Thus, while dust storm polar warmings are relatively brief and exceptional events within the climatology of Mars's atmospheric circulation, they do illustrate two aspects of the circulation important for modeling: (1) the PMOC can exist in the form of a nearly pole-to-pole circulation [*Schneider*, 1983] or at least one that upwells at a displacement from the pole far greater than observed on the Earth; (2) the PMOC, a feature of the lower atmosphere and whose analog on Earth is restricted to the troposphere, can penetrate to a level of the atmosphere that is in radiative equilibrium in an average sense [*Zurek et al.*, 1992], likely has a momentum budget dominated by dissipation of gravity waves and tides [e.g., *Barnes*, 1991], and thus resembles the Earth's mesosphere. This type of circulation can arise because the thermal structure of Mars lacks a highly stable atmospheric layer like the stratosphere to isolate the lower atmospheric circulation from the middle atmospheric circulation. Therefore, current martian general circulation models (GCMs) [e.g., *Wilson and Hamilton*, 1996; *Forget et al.*, 1999; *Takahashi et al.*, 2003; *Moudden and McConnell*, 2005; *Hartogh et al.*, 2005; *Kuroda et al.*, 2005; *Kahre et al.*, 2006; *Richardson et al.*, 2007] generally simulate both the lower and middle atmospheres and are now being coupled with models of the upper atmosphere [e.g., *Angelats i Coll et* *al.*, 2005]. These latter coupled models not only support more accurate simulation of global dust storms but also are useful for quantifying exchange of volatiles between the lower and the upper atmosphere to understand the present, past, and future history of martian atmospheric loss.

Until recently, observational constraints on simulations of the middle atmosphere were limited to ground-based microwave observations [e.g., *Deming et al.*, 1986] and retrievals from infrared limb observations by the Thermal Emission Spectrometer (TES) on Mars Global Surveyor (MGS) [*Smith et al.*, 2001]. These observations suggested that there is a thermal inversion near the winter pole (either north or south) throughout much of the year. This inversion, however, is cooler and at higher altitude than dust storm polar warmings.

New observations by the Mars Climate Sounder (MCS) [*McCleese et al.*, 2007] on Mars Reconnaissance Orbiter (MRO) [*Zurek and Smrekar*, 2007] now are providing information about the thermal structure of Mars over a greater depth of the middle atmosphere than TES and at higher spatial and temporal resolution than ground-based microwave observations. In addition, observations from MCS can be used to retrieve vertical profiles of aerosol, which provide constraints on the lower atmospheric circulation and the forcing of the circulation by radiative heating/cooling due to dust and water ice.

This paper is intended as a companion to McCleese et al. (2010, in preparation), which describes the seasonal cycle of the atmospheric thermal structure and aerosol distributions using retrievals from MCS observations. McCleese et al. (2010) (hereafter, "P1") focuses on Mars Year (MY) 29 (according to the convention of *Clancy et al.* [2000]), a year without a global dust storm, and therefore provides important observational information that can constrain "background" simulations of the martian general circulation. Here I explore the mean meridional circulation of the lower and middle atmospheres at the equinoxes and solstices by integrating analysis of the MCS retrievals at the level presented by McCleese et al. (2010) with general results from both theory and modeling.

2.2 Data

2.2.1 Retrievals

McCleese et al. [2007] describes the MCS instrument and observing strategy. *Kleinböhl et al.* [2009] provides an in-depth description of the first generation retrieval algorithm. At present, atmospheric retrievals from MCS observations provide vertical profiles with respect to pressure, p (Pa), of temperature, T (K), dust opacity, i.e., the extinction per unit height due to dust, $d_z\tau_{dust}$ (km^{-1}) at 463 cm^{-1}, and water ice opacity $d_z\tau_{H_2Oice}$ (km^{-1}) at 843 cm^{-1}. The retrievals used here were generated using a more advanced retrieval algorithm than described in *Kleinböhl et al.* [2009], which includes the effects of aerosol scattering in the radiative transfer.

2.2.2 Zonal Averaging and Sampling

To study the zonal average circulation of the planet, the MCS retrievals and quantities derived from them (as described later in Chapter 2.2) are averaged after being binned by Mars Year (MY), L_s (5° resolution centered at 0°, 5° etc.); time of day: "dayside" (9:00-21:00 LST) and "nightside" (21:00-9:00 LST); mean latitude (5° resolution); and mean longitude (5.625° resolution). The spatial resolution of the binning is chosen to be comparable to standard Mars general circulation model grids. Mean latitude and longitude refer to the coordinates at the tangent point of the limb path observed by the center of the MCS detector array at ~40 km above the surface. Zonal averages are the average of the longitudinal averages in all longitudinal bins containing data.

Figure 2.1 plots the population of retrievals in individual latitudinal-longitudinal bins in the L_s bins corresponding to the equinoxes and solstices (the focus of this study). The nightside at northern summer solstice is most densely sampled (closest to optimal given ideal operation of the instrument, spacecraft, and retrieval algorithm), while the dayside at northern spring equinox is least densely sampled. Undersampling is usually attributed one of two reasons: (1) operational: the instrument is powered off, or the spacecraft is pointed significantly off-nadir; and (2) aerosol opacities are high, due to dust storms and near the equator in all seasons, or due to water ice clouds in northern spring and in the summer in the northern tropics [*Kleinböhl et al*, 2009]. Except for operational impediments, sampling is likely to improve as retrieval algorithms are improved, permitting retrievals under conditions of higher aerosol opacity than at present.

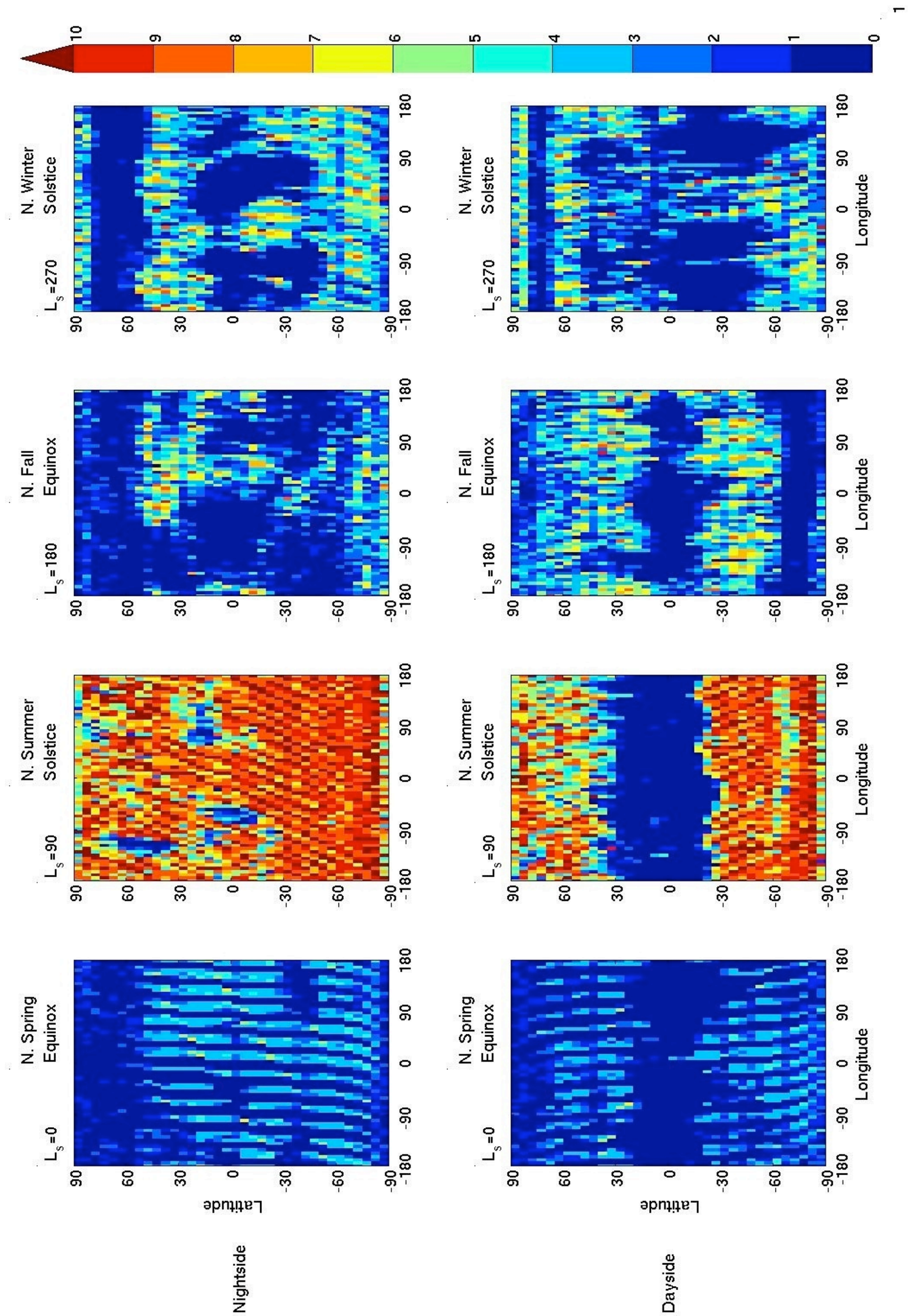

Figure 2.1. Number of retrievals per latitudinal/longitudinal bin for the labeled time of day and L_s bins during MY 29. The color scale is deepest red for 10 retrievals or more.

2.2.3 Winds

An estimate of the zonal gradient wind, $U(p)$, is derived from the zonal average temperature by taking the lowest pressure level with retrieved temperature data in each latitudinal bin as a level of no motion, p_{LNM}, and estimating the thermal wind, $\hat{U}(p)$:

$$\hat{U}(p) = \int_{p_{LNM}}^{p} \frac{R_d}{f} \left(\frac{dT}{dy}\right)_p d\ln p' \tag{2.1}$$

where R_d is the specific gas constant, f is the Coriolis parameter for the latitudinal bin, and $\left(\frac{dT}{dy}\right)_p$ is the temperature gradient at constant pressure. To compute the gradient wind $U(p)$, we iteratively apply Eq. 2.2 to convergence [*Holton*, 2004].

$$U_{n+1}(p) = \frac{U_n}{1 + \frac{\sqrt{U_n^2}}{|fR_M|}} \tag{2.2}$$

where R_M is the radius of Mars. Eqs. 2.1 and 2.2 are only appropriate for winds in approximate geostrophic balance and so cannot be used for diagnosis of zonal winds in the tropics due to the low magnitude of the Coriolis parameter. Therefore, $U(p)$ calculated in the tropics is not plotted.

2.3 Investigative Approach

2.3.1 Use of Zonal Average Plots

Zonal average plots of temperature, zonal wind, and aerosol mass mixing ratio are often used in modeling studies [e.g., *Richardson and Wilson*, 2002] to illustrate aspects of the simulated circulation, particularly the mean meridional circulation. Figures 2.2, 2.3, 2.4, and 2.5 show respectively: the zonal average temperature, the estimated zonal wind, the zonal average dust density scaled opacity (a proxy for dust mass mixing ratio), and the zonal average water ice density scaled opacity (a proxy for water ice mass mixing ratio) on the nightside and dayside at the solstices and equinoxes.

Since longitudinal sampling is minimal in some seasons (Figure 2.1), the zonal averages in Figures 2.2—2.5 are not necessarily accurate. Zonal temperature averages based on even a small number of longitudinal bins should be accurate under most conditions: a consequence of the relative weakness of eddies in comparison to planetary-scale circulations like the non-migrating thermal tides [*Zurek et al.*, 1992]. Dust storm conditions may be an exception. Dust heating aloft may occur faster than the planetary circulation can adjust, while temperatures near the surface are suppressed relative to less dusty areas. Another exception may be the northern hemisphere during the winter, where baroclinic eddy amplitudes are known to be large [*Barnes,* 1980, 1981; *Wilson et al.,* 2002], but this region is better sampled longitudinally. Especial caution is required for analyzing the zonal average aerosol distributions, which are biased toward the dust and water ice distributions over regions with successful retrievals. The high airmass factor of

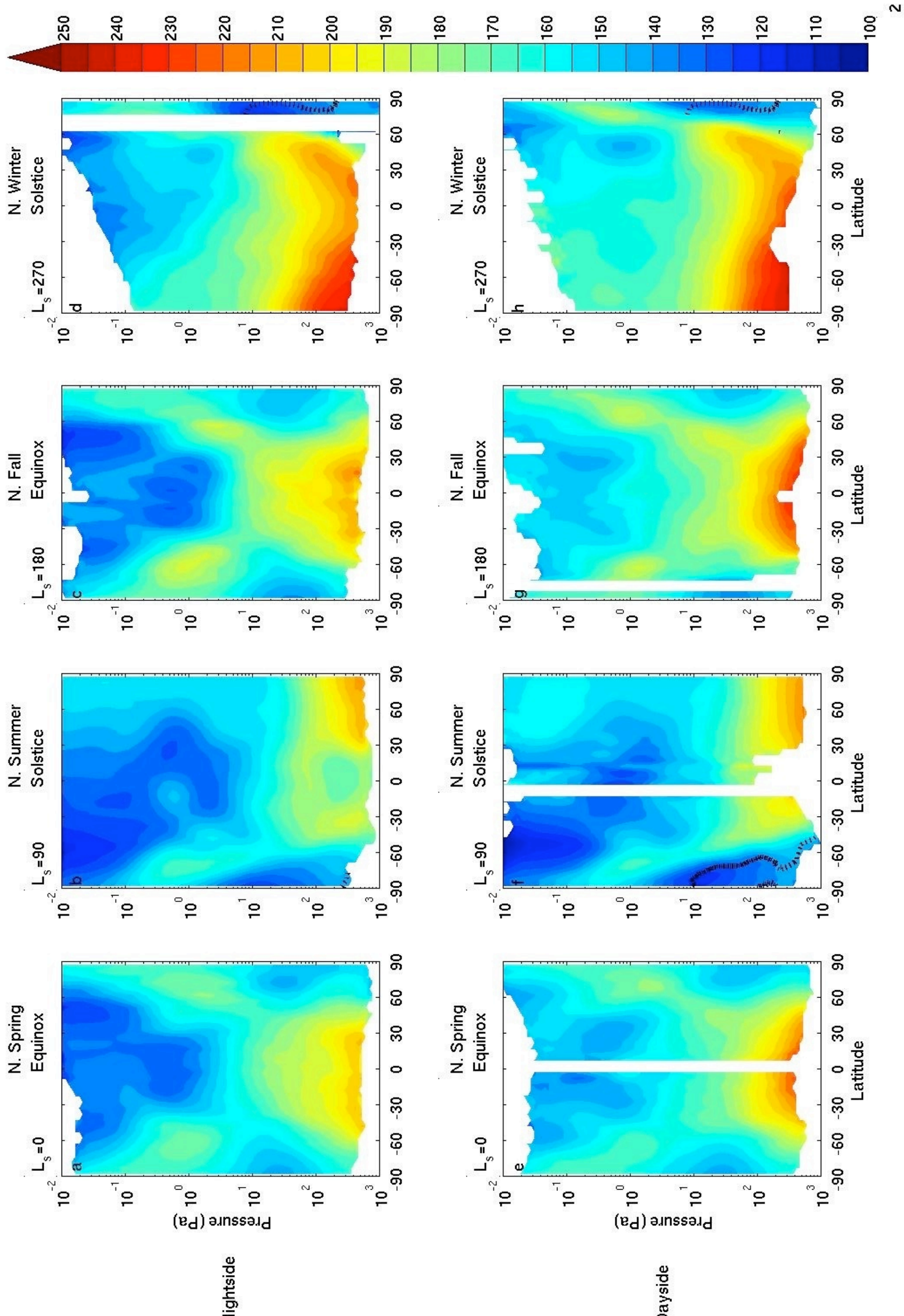

Figure 2.2. Zonal average temperature (K) for the labeled time of day and L_s bins during MY 29. Contours are every 5 K. The black contour indicates the CO_2 frost point.

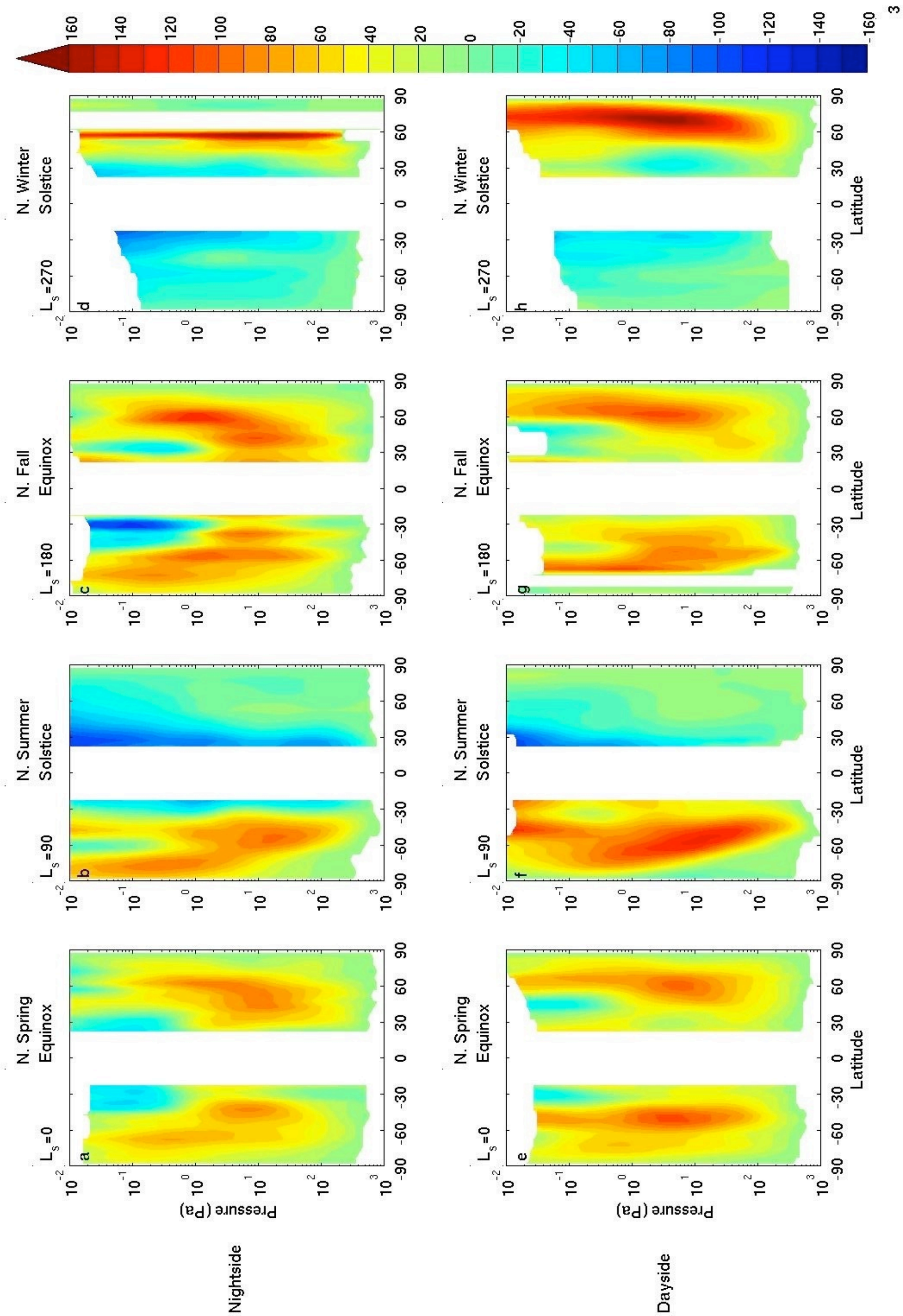

Figure 2.3. Estimated zonal wind velocity (ms^{-1}) for the labeled time of day and L_s bins during MY 29. Contours are every 10 ms^{-1}.

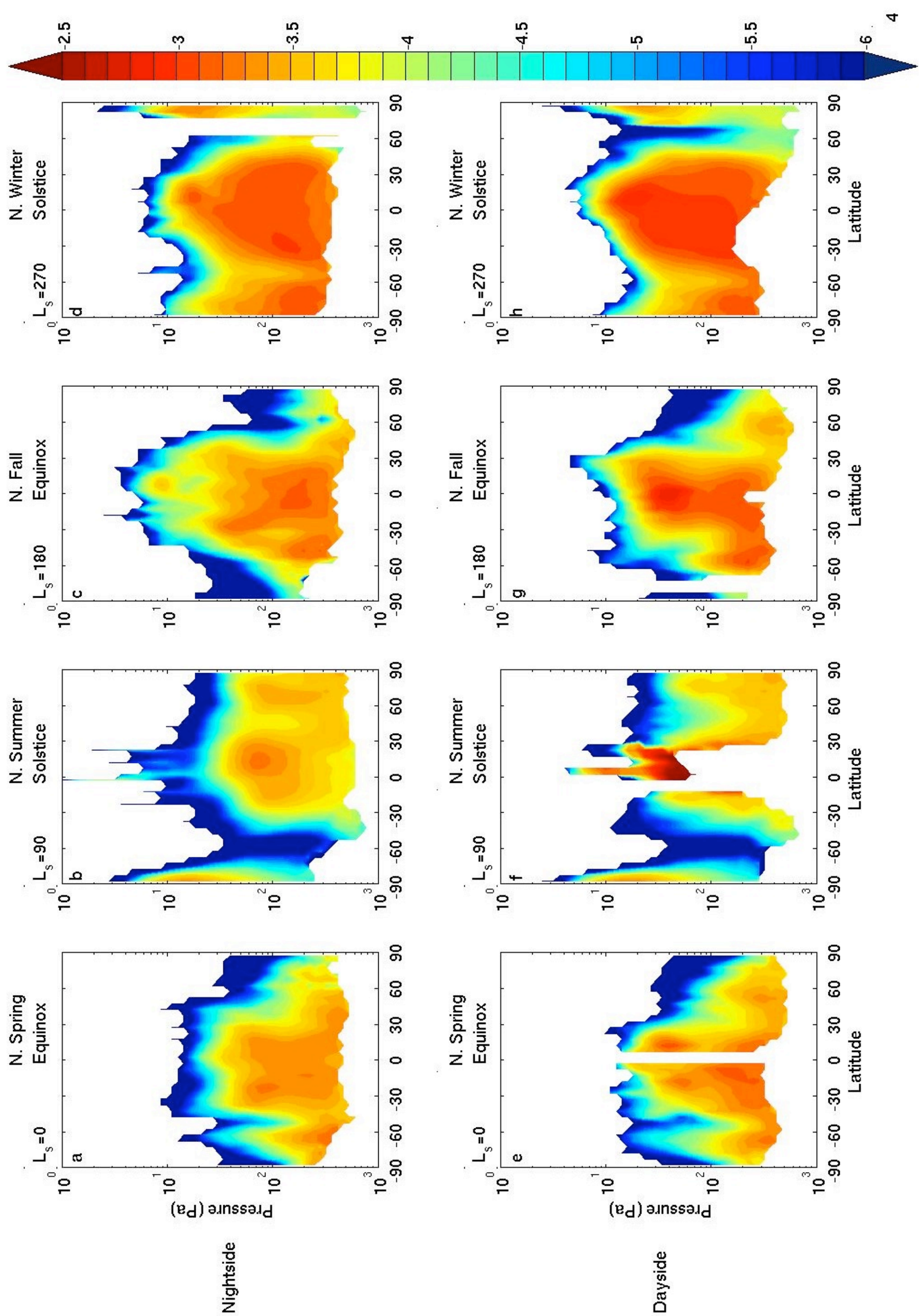

Figure 2.4. Log_{10} of the zonal average dust density scaled opacity ($m^2\ kg^{-1}$) for the labeled time of day and L_s bins during MY 29. Contours are every 0.1 log units.

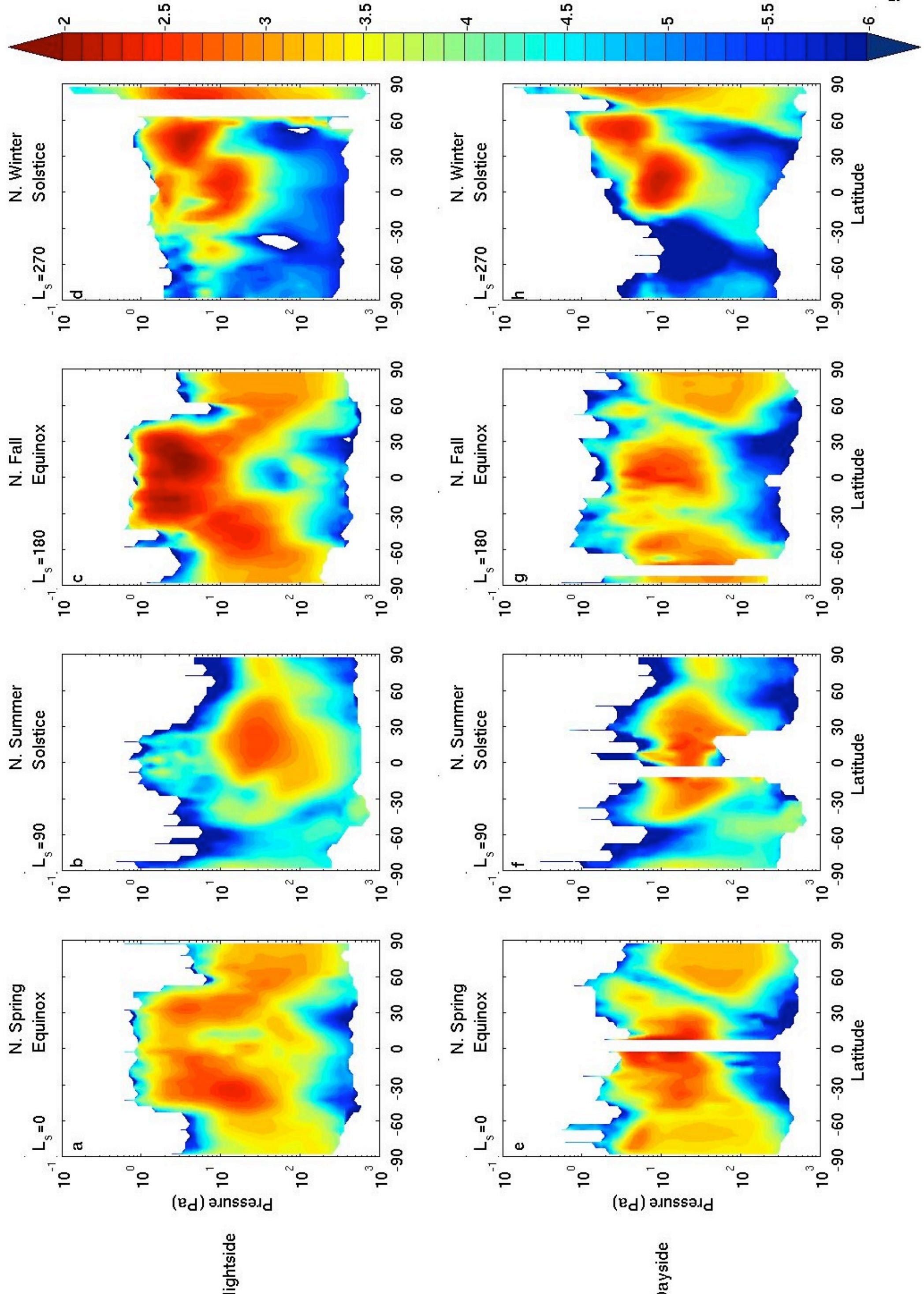

Figure 2.5. Log_{10} of the zonal average water ice density scaled opacity ($m^2\ kg^{-1}$) for the labeled time of day and L_s bins during MY 29. Contours are every 0.1 log units.

MCS limb observations *a priori* makes retrieval success unlikely at high aerosol opacities, systematically biasing the zonal averages toward regions/vertical ranges with low dust/ice opacities.

2.3.2 Qualitative Reconstruction of the Mean Meridional Circulation

The observed thermal structure and aerosol distributions in Figures 2.2—2.5 are the result of multiple, often coupled processes with scales ranging from the global to the microscale. Thus, substantial improvement in our understanding of the mean meridional circulation eventually will rely upon the assimilation of temperature and aerosol concentrations into a general circulation model (GCM) [e.g., *Lewis et al.*, 2007; *Wilson et al.*, 2008] or direct measurements of the wind field.

While eagerly awaiting assimilation-driven modeling of the mean meridional circulation or direct wind measurements over the broad vertical range of the atmosphere observed by MCS, the observations and analysis presented in Figures 2.2—2.5 can be used in combination with insights from theory primarily developed for understanding the atmospheric circulation of the Earth (at the level of *Holton* [2004]) and an ensemble of radiative-convective models of the martian atmosphere [e.g., *Colburn et al.*, 1989; *Joshi et al.*, 1995; *Haberle et al.*, 1997; *Zalucha et al.*, 2010] to develop rough schematics of the mean meridional circulation throughout the lower and middle atmospheres at the equinoxes and solstices.

I first will make direct inferences from the zonal average plots about upwelling, downwelling, and the vigor of meridional and vertical mixing. I then will supplement those direct inferences with insights previously gleaned from theory and modeling to construct qualitative schematics of the mean meridional circulation, indicating where the schematic is ambiguous to motivate future modeling investigations and direct measurements.

Inferring upwelling and downwelling from the thermal structure is primarily an assessment of departure of temperatures from radiative equilibrium. As air is forced to rise (sink) in the atmosphere, it will cool (warm) adiabatically. Therefore, in the absence of diabatic heating by absorption of visible and infrared radiation by aerosols or trace gas species (at least those not included in radiative equilibrium models), temperatures cooler (warmer) than radiative equilibrium directly indicate upwelling (downwelling) driven by dynamical processes.

The vertical distribution of dust in Mars's atmosphere is a measure of the non-surface radiative forcing of atmospheric circulations on all scales and indicative of the meteorological systems that lift dust. (Studies of dust lifting, transport, and radiative forcing are the subject of Chapters 4 and 5; my primary focus here is on the connection between seasonal variability in the dust distribution and seasonal variability in the circulation.) But the global atmospheric circulation also re-distributes lifted dust, so dust can be a useful tracer of the mean meridional overturning circulation, particularly in the lower atmosphere [*Richardson and Wilson*, 2002; *Kahre et al.*, 2006]. Characteristic sedimentation velocities are of the same magnitude as characteristic vertical velocities of the planetary-scale circulation, ~10^{-2} ms^{-1}, so when dust is injected into the atmosphere at presumably higher vertical velocities, it will tend to rise or remain stable in zones of mean upwelling but sink more quickly by its own negative buoyancy in combination with the large-scale flow in zones of mean downwelling. In addition, sedimentation of martian dust is sufficiently slow that dust can be advected thousands of kilometers from where it is lifted [*Murphy et al.*, 1993], making dust a tracer of both horizontal and vertical flows on timescales shorter than its atmospheric residence time. However, this method of inference is complicated by the dependence of the sedimentation velocity on air density and particle size. The sedimentation velocity increases with height, so dust may not be fully distributed through a region of positive vertical velocity. Other complications include the potential removal or obscuration of dust by condensation of water ice or carbon dioxide ice.

The vertical distribution of water ice in the atmosphere constrains the vertical profile of water vapor and radiative forcing by water ice. Water ice thus can be a tracer of moist air at temperatures sufficiently cold for saturation and the path of water vapor from its sources (mainly warming water ice caps at the poles), which is controlled in part by the mean meridional circulation. In the simulations of *Richardson et al.* [2002], a water ice maximum over the northern tropics originates from water vapor coming from the northern (summer) pole near the surface and then strongly upwelling into colder atmosphere at ~150 Pa. Following this result, we will infer that an area with high concentrations of water ice spanning a strong vertical temperature gradient is a zone of upwelling. Such an inference can be complicated by variations in available condensation nuclei and advection, diffusion, and sedimentation of water ice. In addition, sublimating water ice in the atmosphere can be a source of water vapor. *Hinson and Wilson* [2004] and *Lee et al.* [2009], however, point out that if the water ice distribution is tidally controlled, the effects of advection, diffusion, and sedimentation can be mostly neglected.

2.4 The Mean Meridional Circulation at the Equinoxes

2.4.1 Description of Thermal Structure and Aerosol Distributions

The principal exceptions to the general hemispheric symmetry of the thermal structure at northern spring equinox (Figures 2.2a and 2.2e) are the temperature minima near poles (which I call the "polar vortices" though vorticity is not diagnosed here.) The winter leaving north polar vortex extends from the remnant cold surface to pressures near 10 Pa. The surface and lower atmosphere are warmer in the south, and so confine the vertical extent of the southern polar vortex. At northern fall equinox (Figures 2.2c and 2.2g), the thermal structure is very similar to northern spring equinox, except that the high latitudes at ~1 Pa and the tropics at ~10 Pa are warmer. The estimated zonal wind distribution at both equinoxes consists of two zonal jets in the mid-latitudes.

The dust distributions at both equinoxes are relatively symmetric about the equator. Dust density scaled opacity is higher and dust penetrates to higher altitudes near the equator than at the poles (Figures 2.4a, 2.4c, 2.4e, and 2.4h). Dust appears to penetrate to lower pressure levels in the tropics at northern fall equinox than at northern spring equinox.

The water ice distributions at both equinoxes differ between day and night due to the influence of the thermal tides [*Lee et al.*, 2009]. They, however, are broadly similar at the same time of day. The clearest difference appears on the nightside, where the layer of water ice in the tropics between 1 and 10 Pa is up to an order of magnitude higher in density scaled opacity at northern fall equinox than northern spring equinox.

Thus, while there are some second-order differences, the thermal structure and aerosol distributions at both equinoxes are sufficiently similar that their qualitative mean meridional circulations will be effectively interchangeable.

2.4.2 Diagnosis of Upwelling and Downwelling

Figures 2.6a-c re-plot zonal average nightside temperature (Figure 2.2a), dust density scaled opacity (Figure 2.4a), and water ice density scaled opacity (Figure 2.5a) for northern spring equinox with upward and downward (solid for definite, dashed for ambiguous) arrows to indicate zones of upwelling and downwelling inferred from the zonal average fields. At the equinox, the temperature maxima of the polar warmings are ~170 K, and from the ensemble of model we see that it is at least 35 K above radiative equilibrium temperatures. Importantly, significant amounts of ice or dust are absent from

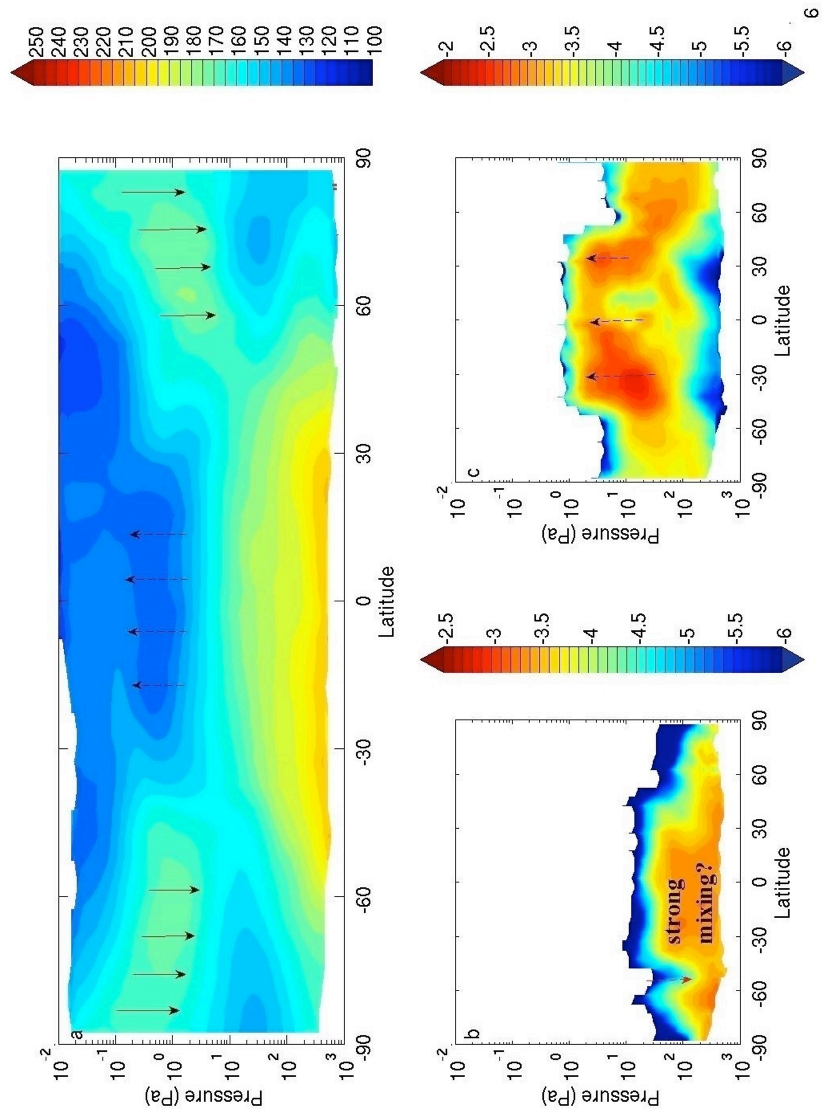

Figure 2.6. Characteristic zonal average fields for an equinoctial case (L_s=0°, nightside) with inferred zones of upwelling (upward arrows), downwelling (downward arrows), and vigorous mixing (label) indicated. Definite inferences are marked with solid arrows. More ambiguous inferences are marked with dashed arrows. The color of arrows is for sake of clarity and has no other significance: (a) temperature (K), identical to Figure 2.2a; (b) dust density scaled opacity ($m^2\ kg^{-1}$), identical to Figure 2.4a; (c) water ice density scaled opacity ($m^2\ kg^{-1}$), identical to Figure 2.5a.

the warmings and the magnitudes of the temperature maxima are fairly similar between the dayside and nightside, thus excluding the possibility that diabatic heating of aerosol is driving the strong departure from radiative equilibrium. Instead, dynamically driven downwelling is indicated.

Nightside temperatures at ~1 Pa in the tropics are ~130 K and dayside temperatures are ~150 K, a variation likely driven by the tides [*Lee et al*., 2009]. The average temperature is thus at least 10 K below radiative equilibrium. Water ice is present at the lower end of this zone of very cold temperatures, but water ice will absorb infrared radiation from below, re-emit it at a lower temperature, and produce a net diabatic heating, which cannot explain why temperatures are cooled below radiative equilibrium.

Dust density scaled opacities at 200 Pa are relatively similar from pole to pole, but the vertical extent of dust at these density scaled opacities is significantly deeper than elsewhere from 40° S to 25° N, indicating strong vertical and meridional mixing in the lower atmosphere at these latitudes. There is a minimum in dust density scaled opacities at ~50° S at 100 Pa. We infer that this minimum is probably not an effect of scavenging by water but due, instead, to downwelling, since ice density scaled opacities at this latitude and level are relatively similar to ice density scaled opacities at this level at higher latitudes, where the vertical extent of dust is deeper.

High ice density scaled opacities are observed over a broad vertical range centered at ~10 Pa at between 45° S and 45° N, which is a region with a vertical temperature gradient. We therefore infer broad upwelling at this level and region.

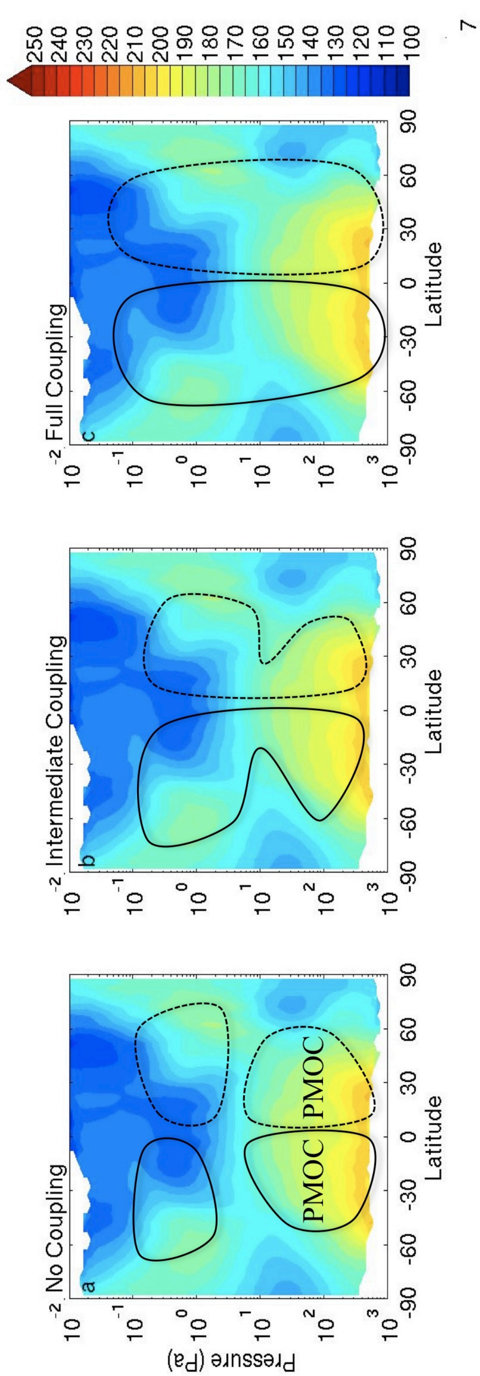

Figure 2.7. Characteristic temperature fields for the equinoctial case: (a, b, and c) as in Figure 2.6 marked with schematic streamlines of the inferred mean meridional circulation for three possible states of coupling as labeled over the boxes in each column. The solid streamlines indicate counter-clockwise flow and the dashed streamlines indicate clockwise flow.

The upwelling and downwelling zones identified here are consistent with meridional cells symmetric about the equator in both the lower and middle atmospheres that rise at the equator and sink at higher latitudes. In the lower atmosphere, the average insolation is strongest at the equator, so the differential heating between the equator and pole creates an unstable flow regime due to incompatibility between radiative equilibrium and angular momentum conservation. To resolve this instability, equatorial air rises from the surface and moves poleward. This air cools at higher latitudes, sinks, and becomes a return flow back to the equator, forming two meridional circulation cells symmetric about the equator: the PMOCs. In the middle atmosphere, theory and modeling suggest that similar cells can be driven by dissipation of waves and tides or aerosol diabatic forcing [e.g., *Holton et al.*, 1995; *Forget et al.*, 1999; *Forbes and Miyahara*, 2006; *Hartogh et al.*, 2007; *Wilson et al.*, 2008].

It is, however, unclear to what extent the lower and middle atmospheric meridional cells are coupled kinematically. Different possible scenarios consistent with the inferred upwelling and downwelling are illustrated on the same temperature plot as Figure 2.6a in Figures 2.7a-c. The lower and middle atmospheric cells in one hemisphere may be fully kinematically coupled in a single cell, in which air rises at the equator into the middle atmosphere, strongly descends within the middle atmospheric polar warming to the surface (Figure 2.7c). Or the lower atmospheric meridional cell may be separated from the middle atmospheric meridional cell by a region of weak vertical motion (opposite to the mutual upwelling or downwelling in the cells) (Figure 2.7a). In the former case, there would be substantial mixing of constituents both meridionally and vertically. In the latter case, mixing would be primarily meridional, isolating the lower from the middle atmosphere (and by extension, the upper atmosphere) with implications for the atmospheric loss of water vapor and other constituents. I note that a Mars GCM simulation of this season [*Forget et al.*, 1999, Figure 10] suggests the local temperature maxima of the polar warmings are consistent with an intermediate state of coupling (Figure 2.7b), in which the PMOC extends deeply into the middle atmosphere in the tropics, is pulled poleward more strongly in the middle atmosphere than in the lower atmosphere by whatever is forcing the middle atmospheric meridional cell, and returns to the deep tropical PMOC in the middle atmosphere. Thus, the PMOC in the model is kinematically coupled with the mean meridional cell in the middle atmosphere in the tropics but not at higher latitudes.

2.5 The Mean Meridional Circulation at the Solstices

2.5.1 Description of Thermal Structure and Aerosol Distributions

The thermal structure and aerosol distributions at northern summer and northern winter solstices differ significantly. Temperatures throughout the atmosphere (except in the polar vortex) are considerably warmer at northern winter solstice than northern summer solstice (Figures 2.2b, 2.2d, 2.2f and 2.2h). In the lower atmosphere (p >10 Pa) at northern winter solstice, temperatures are usually highest in the southern high latitudes, are lower toward the tropics, and have a secondary maximum in the northern mid-latitudes that tilts poleward at lower pressures. This qualitative thermal structure is only weakly apparent at northern summer solstice. In the middle atmosphere, there is a temperature maximum at ~1 Pa near the winter pole at both solstices, which is slightly warmer at northern winter solstice. The estimated zonal wind structures are qualitatively similar at both solstices and consist of a strong westerly jet (stronger at northern winter solstice) in the mid-high latitudes of the winter hemisphere and weak westerlies or easterlies in the mid-high latitudes of the summer hemisphere (Figures 2.3b, 2.3d, 2.3f and 2.3h).

At both solstices, dust is primarily restricted to the summer hemisphere and winter hemisphere tropics (Figures 2.4b, 2.4d, 2.4f and 2.4h). A region of extremely dust clear air generally separates the dust in the winter tropics from the dust in the winter high latitudes (likely CO_2 ice being retrieved as dust). This region of dust clear air is broader at northern summer solstice. In the winter tropics and summer hemisphere, dust density scaled opacity is higher at northern summer solstice. The summer hemisphere and tropical dust distributions at the northern summer and northern winter solstices also differ in stratification. Dust density scaled opacity is constant or decreases with height at northern winter solstice but tends to increase with height in the tropics below 60 Pa at northern summer solstice.

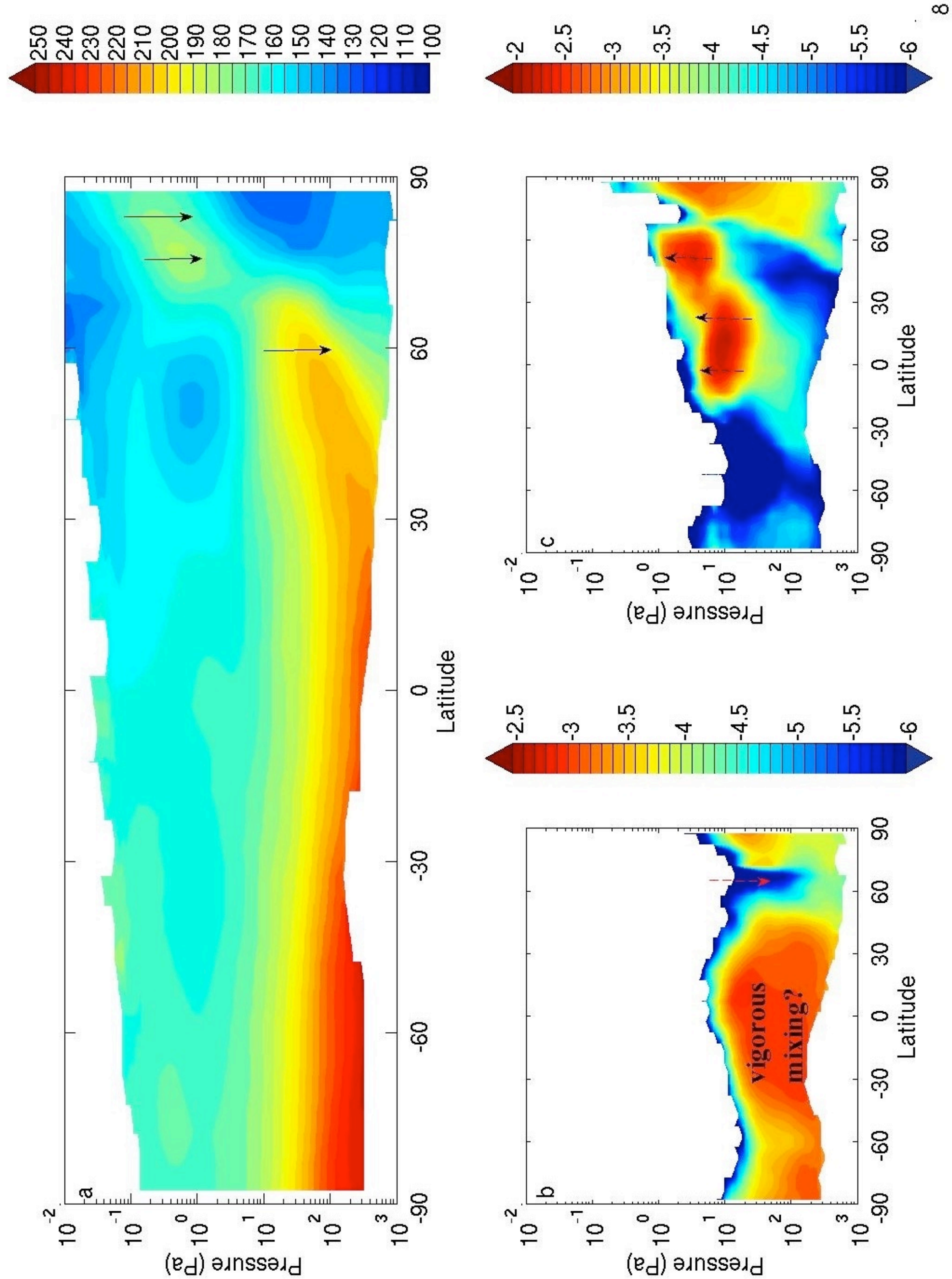

Figure 2.8. As Figure 2.6 but for northern winter solstice (L_s=270º, dayside).

The water ice distributions at the solstices differ significantly (Figures 2.5b, 2.5d, 2.5f and 2.5h). The northern summer solstice distribution is dominated by a high density scaled opacity layer of water ice in the northern tropics at ~30 Pa, but smaller amounts of water ice are present at all latitudes at $p > 10$ Pa. At northern winter solstice, the thickest layers of water ice are restricted to the summer hemisphere at $p < 10$ Pa. Note that water ice density scaled opacity is higher in the winter polar vortex at northern winter solstice.

Due to differing topography and summer insolation between the northern and southern hemispheres, the southern summer solstitial circulation (at least the PMOC) is believed to be more vigorous than its northern analog [*Zurek et al.,* 1992; *Richardson and Wilson*, 2002; *Takahashi et al.*, 2003]. Because of this prior knowledge and the significant differences in thermal structure and aerosol distributions between the two solstices in Figures 2.2—2.5, the circulation at each solstice will be considered separately.

2.5.2 Diagnosis of Upwelling and Downwelling

Figures 2.8a-c re-plot zonal average dayside temperature (Figure 2.2g), dust density scaled opacity (Figure 2.3g), and water ice density scaled opacity (Figure 2.4g) for southern summer solstice with arrows indicating upwelling and downwelling as in Figures 2.6a-c. The temperature of the middle atmospheric polar warming near the north pole is ~180 K. Because the temperature of this warming exceeds temperatures at this level at all other latitudes, it can be inferred to be much warmer than radiative equilibrium even without consulting a model. Comparison with the ensemble of models, (see particularly *Haberle et al.* [1997]) suggests the departure from radiative equilibrium of the observed warming is at least 70 K. The warming is above the level of high ice concentrations and is at latitudes with no or limited solar insolation at this season, so downwelling is inferred. In the lower atmosphere, there is substantial temperature inversion at a level of ~50 Pa at 60° N. Comparison with the model of *Haberle et al.* [1997] suggests the departure from radiative equilibrium of the observed warming is at least 50 K. This region is mostly free of water ice and dust and just on the edge of the noon terminator, which suggests diabatic heating is minimal, so downwelling is inferred.

Dust density scaled opacities are high and roughly constant with pressure at pressures greater than 20 Pa from 40° to 30° N, indicating strong vertical and meridional mixing in the lower atmosphere at these latitudes. There is a minimum in dust concentration at ~60° N at 100 Pa (that continues to the pole if the dust there is CO_2 ice). Water ice concentrations at this latitude and level are higher than at lower latitudes, so this minimum could be as easily due to scavenging as it could be due to downwelling.

Water ice concentrations are high in a tilting region stretching from a level of ~100 Pa at 30° S to a level of ~3 Pa at 50° N. Temperatures decrease with height throughout this latitudinal band. If we interpret this feature as due to gradual drying of vapor-rich air from the summer pole upwelling across the equator, we may infer broad upwelling throughout this latitudinal band.

The upwelling and downwelling zones identified here are consistent with single meridional cells in the lower and the middle atmospheres. The lower atmosphere cell (the PMOC) rises in the southern mid-latitudes and sinks at 60° N. The theory of *Lindzen and Hou* [1988] suggests the latitude of PMOC downwelling corresponds to the latitude of upwelling in the opposite hemisphere, but there is no definite confirmation of this idea from the observations. In the middle atmosphere, the downwelling near the pole indicates a middle atmospheric cell, but it is unclear from the observations whether the upwelling of this cell takes the form of weak upwelling in the middle atmosphere from the summer pole to the winter mid-latitudes or instead manifests as stronger, more localized upwelling in some particular latitudinal band.

The discontinuity between the warming due to downwelling in the lower atmosphere near 60° N and the warming due to downwelling in the middle atmosphere near the north pole suggests that the PMOC in the lower atmosphere is not fully kinematically coupled with the meridional cell in the middle atmosphere. The polar warming in a simulation of the circulation in this season by the Mars GCM used in Chapter 2.4.2 [*Forget et al.*, 1999, Figure 7] is 50 K warmer than the observed polar warming. In this simulation, the meridional mass streamfunction is consistent with nearly complete coupling between the PMOC and the mean meridional cell in the middle atmosphere, since the streamlines of the PMOC in the northern high latitudes remain vertical as low as 15 km above the surface (as opposed to 55 km in the equinoctial case). Because of the similarity between the temperature of the polar warming simulated by *Forget et al.* [1999] and observed dust storm polar warmings, it is possible that dust

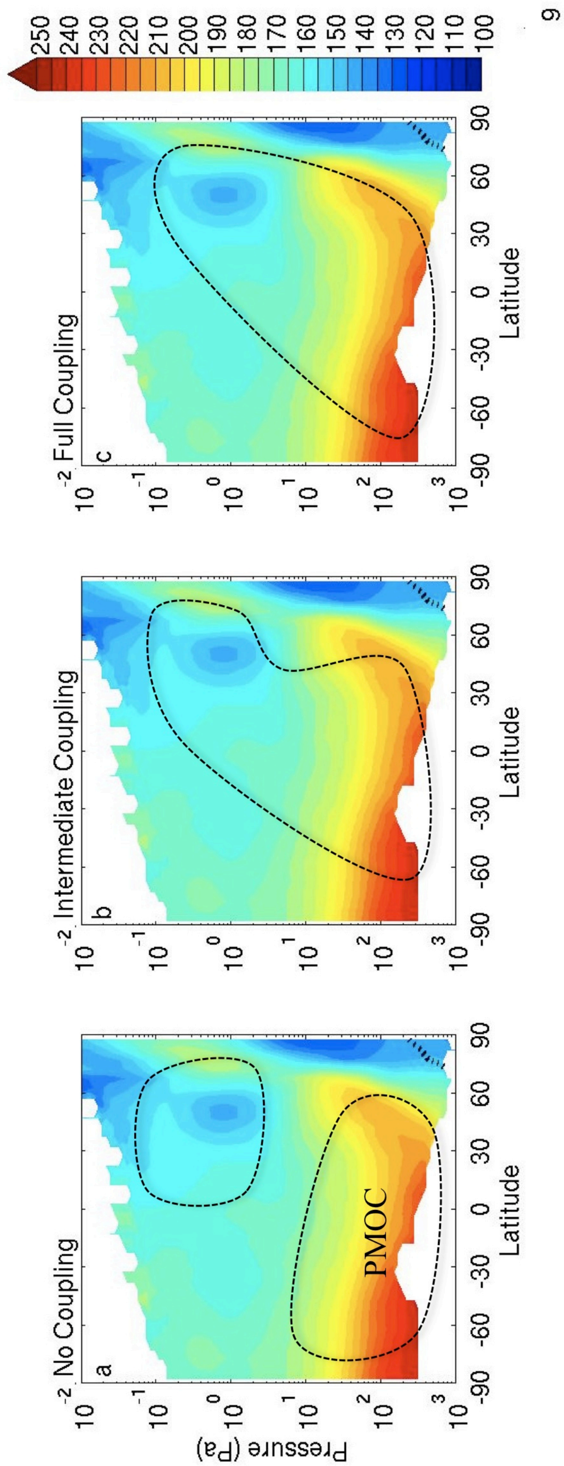

Figure 2.9. As Figure 2.7 but for northern winter solstice.

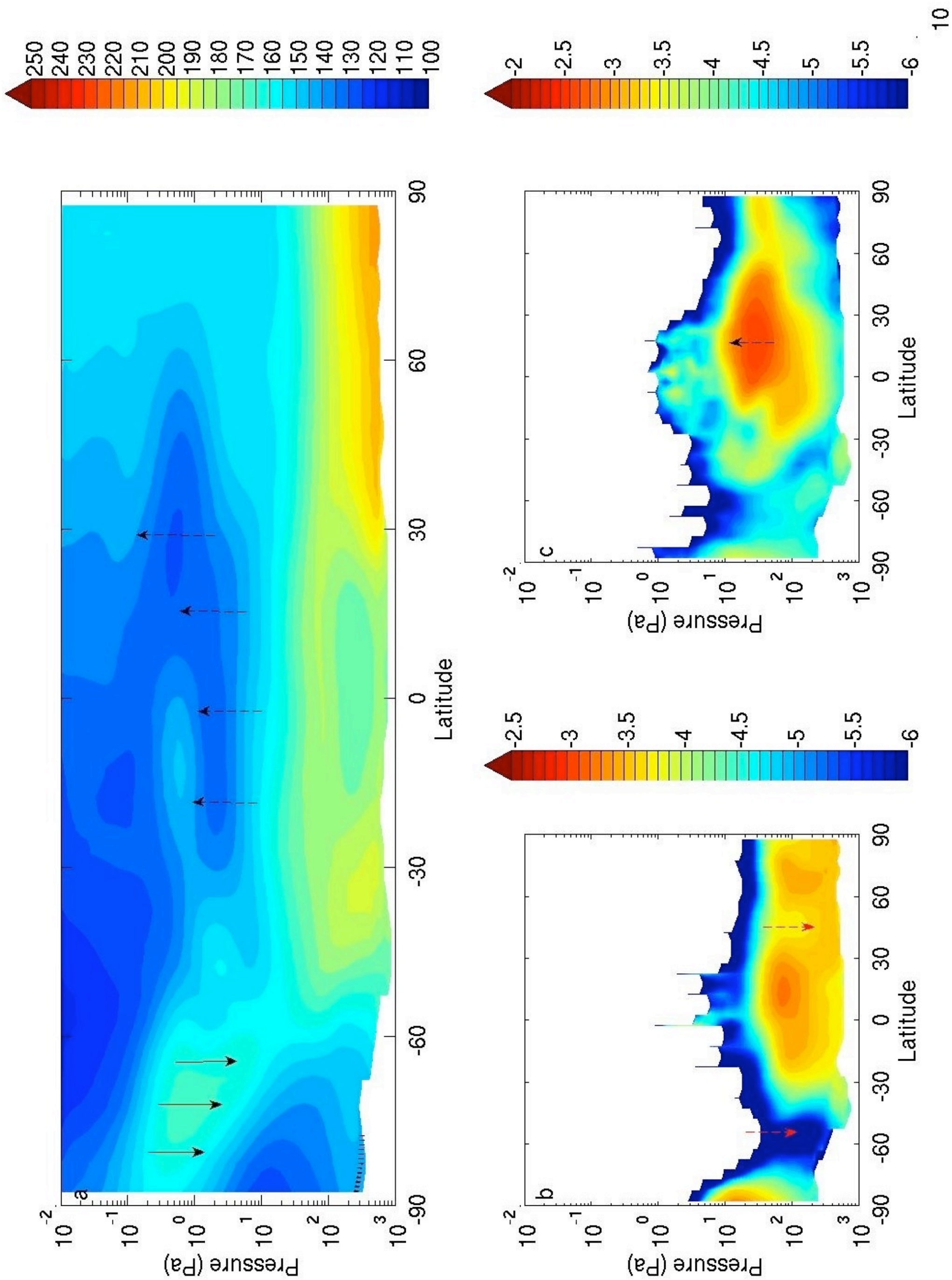

Figure 2.10. As Figure 2.6 but for the northern summer solstice (L_s=90º, nightside).

storm polar warmings are the result of a fully kinematically coupled lower and middle atmospheric meridional circulation. The mean meridional circulations in the simulations of *Wilson et al.* [1997] and *Kuroda et al.* [2009] are consistent with this idea.

From the observations alone, little can be inferred about the vertical structure of tropical upwelling. So I cannot determine whether the lower and middle atmospheric meridional cells are in an intermediate state of coupling or fully decoupled. Figures 2.9a-c show possible structures of the mean meridional cells for different states of kinematic coupling.

The dust-clear air in the winter high-latitudes is consistent with the area of the atmosphere heated by downwelling in the lower atmospheric PMOC. On the poleward side of the vortex wall, water ice opacities increase again (Benson et al., submitted to *J. Geophys. Res.*), but density scaled opacities are much lower than in the tropical cloud belt. The southern winter atmosphere is seen to be much clearer than the northern winter atmosphere, consistent with Mars Odyssey Gamma Ray Spectrometer argon observations [*Sprague et al.,* 2007] that suggest that the southern polar vortex is much more dynamically isolated than that of the north.

Figures 2.10a-c re-plot zonal average nightside temperature (Figure 2.2b), dust density scaled opacity (Figure 2.3b), and water ice density scaled opacity (Figure 2.4b) for southern summer solstice with arrows indicating upwelling and downwelling as in Figures 2.6a-c and 2.8a-c. The temperature of the middle atmospheric polar warming near the south pole is ~170 K (Figure 2.10a). Because the temperature of this warming exceeds temperatures at this level at all other latitudes, it can be inferred to be much warmer than radiative equilibrium even without consulting a model. The full ensemble of radiative-convective models (particularly *Zalucha et al.* [2010]) suggests temperatures exceed radiative equilibrium by at least 35 K. The region of warming is free of aerosol, so downwelling is inferred. Temperatures at ~1 Pa in the tropics average ~135 K. The average temperature is thus at least 20 K below radiative equilibrium [*Colburn et al.*, 1989], so upwelling is inferred there.

Downwelling is inferred in the vicinity of the region of dust-clear air at 60° S and ~100 Pa (Figure 2.10b), though downwelling also likely occurs significantly equatorward of this latitude, where there is a maximum in temperature and a minimum in water ice, possibly indicating a region of adiabatic warming. Dust density scaled opacity has a notable minimum at ~45° N and ~100 Pa. Since water ice density scaled opacity at this pressure level is higher in the southern tropics than in this region, enhanced scavenging by water ice is not a convincing explanation for the minimum, so downwelling is inferred there. Water ice concentrations are highest at ~30 Pa over the northern tropics (Figure 2.10c). Temperatures are decreasing with altitude at this pressure level. If this feature is due to condensation of vapor rich air from the summer pole upwelling in the northern tropics, broad upwelling throughout this latitudinal band may be inferred.

Thus, the inferred circulation in the lower atmosphere consists of two PMOCs that upwell in the northern tropics: a stronger, broader cell that downwells in the southern mid-latitudes and a weaker, narrower cell that sinks in the northern mid-latitudes. In the middle atmosphere, another cell likely upwells through the tropics and downwells near the winter pole. As at southern summer solstice, observations argue against full kinematic

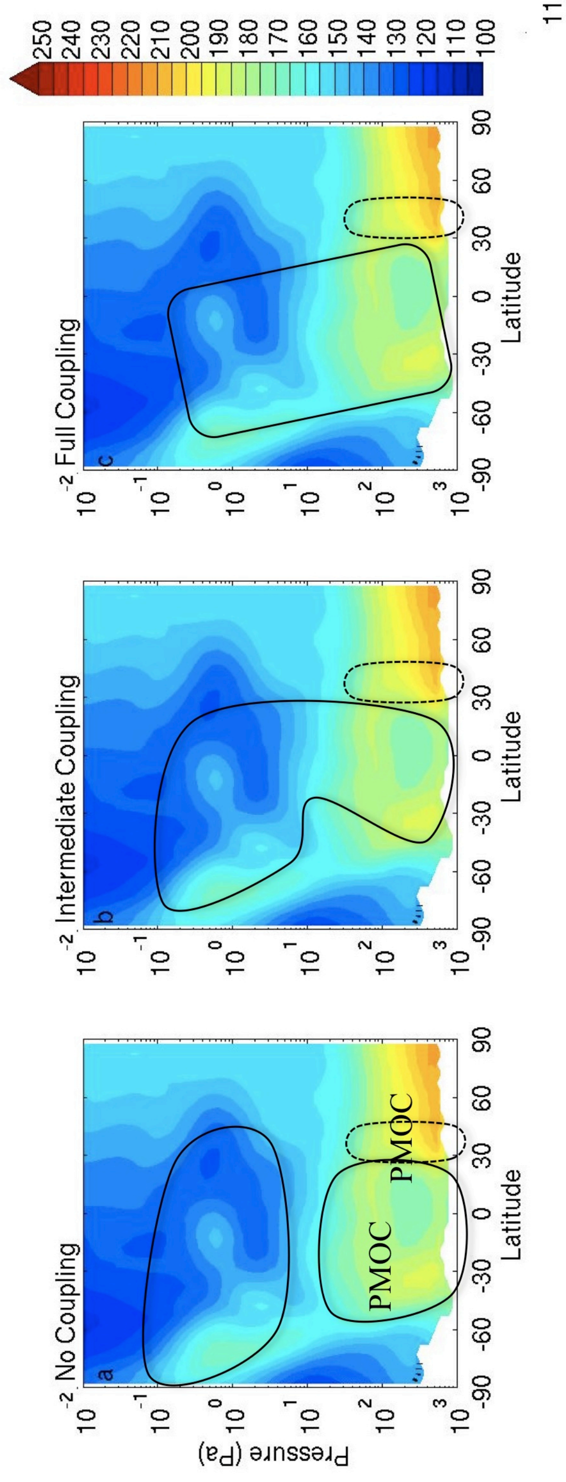

Figure 2.11. As Figure 2.7 but for the northern summer solstice.

coupling, but the exact degree of kinematic coupling cannot be determined. Possible options are plotted in Figures 2.11a-c. Note that a Mars GCM simulation of this season [*Hartogh et al.*, 2007] simulates a similar thermal structure and a circulation in which the PMOC and a middle atmospheric meridional cell are partially coupled.

2.6 An Alternative Approach to the Analysis of Kinematic Coupling

As noted by *Wallace and Hobbs* [1976], planetary atmospheres act like heat engines "in a gross, statistical sense," in which energy is concentrated by solar absorption in the lower atmosphere of the tropics and summer hemisphere and re-distributed by circulations like the PMOC toward cooler air at higher altitudes and latitudes. Thus, the generation of mechanical energy to maintain atmospheric circulations depends on the positive thermodynamic efficiency of the atmospheric heat engine implied by this general effective diffusion of heat

Thus, complete kinematic decoupling of the lower and middle atmospheric mean meridional circulations is unlikely to produce a middle atmosphere in which the equator is substantially cooler than the pole. The middle atmospheric cell in that case would be a thermally indirect circulation equivalent to a heat engine running strongly in reverse. The negative efficiency at northern summer solstice would be ~25%. Such a circulation would need to be sustained entirely by dissipation as heat of waves and tides propagating into the middle atmosphere from below, since waves and tides are ultimately driven by diabatic heating in the lower atmosphere. The analysis in Chapter 3 suggests that zonal average direct heating by gravity wave dissipation in the middle atmosphere is 1 K or less. Unless dissipation by tides or other types of waves is substantially larger, this gradient must be sustained by effective eddy diffusion of heat from the tropical lower atmosphere.

In that case, the lower and middle atmospheric mean meridional circulations must be at least partially coupled throughout the year. Coupling can be assessed quantitatively by balancing eddy diffusion against the net excess radiation in the middle atmosphere due to the polar warming and the equatorial cooling. For example, high effective eddy diffusivities according in such a scheme likely would occur in dust storm polar warmings and so would indicate nearly full coupling. Such an analysis is beyond the scope of this study.

2.7 Summary

The first simultaneous and systematic observations of the thermal structure and aerosol distributions of lower and middle martian atmospheres to above 80 km have been used to perform a simple, qualitative analysis of the background seasonal variability of the mean meridional circulation. This analysis provides evidence of a vigorous and clearly delineated middle atmospheric circulation at all seasons of the year. Because this circulation maintains a strong positive equator to pole gradient in temperature, it is thermodynamically implausible without invoking some amount of kinematic coupling between the circulations of the lower and middle atmospheres. However, in all cases during the year analyzed, the coupling is much weaker than indicated by GCM simulations of dust storm polar warmings.

As the retrieval algorithm improves, an increased volume of data from higher aerosol opacity locations and seasons will become available, allowing the meteorology of cloud systems and dust storms and interannual variability to be studied in more detail. Further downstream, MCS information on the spatial distribution of temperature and aerosol radiative heating offers the best opportunity for assimilation of spacecraft data, potentially yielding “reanalysis” data for Mars, as is now standard for Earth science. The quality and detail of the MCS data suggest that a new range of problems within martian meteorology now can be attacked with a combination of data and atmospheric modeling. Much as atmospheric modeling over the last decade has found a need for an extended vertical range, the MCS observations argue strongly that future observations of the atmosphere for the purpose of meteorology and climate should at least match the MCS observational vertical range and resolution for temperature and aerosols.

Bibliography

Angelats i Coll, M., F. Forget, M. A. López-Valverde, and F. González-Galindo (2005), The first Mars thermospheric general circulation model: The Martian atmosphere from the ground to 240 km, *Geophys. Res. Lett.*, *32*, L04201, doi:10.1029/2004GL021368.

Barnes, J.R. (1980), Time spectral analysis of midlatitude disturbances in the Martian atmosphere, *J. Atmos. Sci.*, *37*, 2002-2015.

Barnes, J.R. (1981), Midlatitude disturbances in the Martian atmosphere: a second Mars year, *J. Atmos. Sci.*, *38*, 225-234.

Barnes, J.R. (1991), A simple nearly analytic model of a gravity wave driven middle atmospheric circulation, *J. Atmos. Sci.*, *48*, 225-235.

Clancy, R. T., B. J. Sandor, M. J. Wolff, P. R. Christensen, M. D. Smith, J. C. Pearl, B. J. Conrath, and R. J. Wilson (2000), An intercomparison of ground-based millimeter, MGS TES, and Viking atmospheric temperature measurements: Seasonal and interannual variability of temperatures and dust loading in the global Mars atmosphere, *J. Geophys. Res.*, *105*(E4), 9553–9571.

Colburn, D.S., J.B. Pollack, and R.M. Haberle (1989), Diurnal Variations in Optical Depth at Mars, *Icarus*, *79*, 159-189.

Deming, D., M. J. Mumma, F. Espenak, T. Kostiuk, and D. Zipoy (1986), Polar warming in the middle atmosphere of Mars, *Icarus*, *66*, 366-379.

Forbes, J.M., and S. Miyahara (2006), Solar Semidiurnal Tide in the Dusty Mars Atmosphere, *J. Atmos. Sci., 63* (7), 1798-1817.

Forget, F., F. Hourdin, R. Fournier, C. Hourdin, O. Talagrand, M. Collins, S.R. Lewis, P.L. Read and J.-P. Huot (1999), Improved general circulation models of the Martian atmosphere from the surface to above 80 km, *J. Geophys. Res 104*, 24155–24175.

Haberle, R.M., C.B. Leovy, and J.M. Pollack (1982), Some effects of global dust storms on the atmospheric circulation of Mars, *Icarus*, *50*, 322-367.

Haberle, R.M., J.B. Pollack, J.R. Barnes, R.W. Zurek, C.B. Leovy, J.R. Murphy, J. Schaeffer, and H. Lee (1993), Mars atmospheric dynamics as simulated by the NASA/Ames general circulation model I. The zonal mean circulation, *J. Geophys. Res., 98*, 3093-3124.

Haberle, R. M., H. Houben, J. R. Barnes, and R. E. Young (1997), A simplified three-dimensional model for Martian climate studies, *J. Geophys. Res.*, *102*(E4), 9051–9067.

Hartogh, P., A. S. Medvedev, T. Kuroda, R. Saito, G. Villanueva, A. G. Feofilov, A. A. Kutepov, and U. Berger (2005), Description and climatology of a new general circulation model of the Martian atmosphere, *J. Geophys. Res.*, *110*, E11008, doi:10.1029/2005JE002498.

Hartogh, P., A.S. Medvedev, and C. Jarchow (2007), Middle atmosphere polar warmings on Mars: Simulations and study on the validation with sub-millimeter observations, *Planet. Space. Sci.*, *55* (9), 1103-1112.

Hinson, D. P., and R. J. Wilson (2004), Temperature inversions, thermal tides, and water ice clouds in the Martian tropics, *J. Geophys. Res.*, *109*, E01002, doi:10.1029/2003JE002129.

Holton, J.R. (2004), *An Introduction to Dynamic Meteorology*, 4th ed., 535 pp. Elsevier, Amsterdam.

Holton, J.R. P.H. Haynes, M.E. McIntyre, A.R. Douglass, R.B. Rood, and L. Pfister (1995), Stratosphere-Troposphere Exchange, *Rev. Geophys.*, *33* (4), 404-439.

Jakosky, B.M. and T.Z. Martin (1987), Mars: North-polar atmospheric warming during dust storms, *Icarus 72*, 528–534.

Joshi, M. M., S. R. Lewis, P. L. Read, and D. C. Catling (1995), Western boundary currents in the Martian atmosphere: Numerical simulations and observational evidence, *J. Geophys. Res.*, *100*(E3), 5485–5500.

Kahre, M. A., J. R. Murphy, and R. M. Haberle (2006), Modeling the Martian dust cycle and surface dust reservoirs with the NASA Ames general circulation model, *J. Geophys. Res.*, *111*, E06008, doi:10.1029/2005JE002588.

Kleinböhl , A., J. T. Schofield, D. M. Kass, W. A. Abdou, C. R. Backus, B. Sen, J. H. Shirley, W. G. Lawson, M. I. Richardson, F. W. Taylor, N. A. Teanby, and D. J. McCleese (2009), Mars Climate Sounder limb profile retrieval of atmospheric temperature, pressure, dust, and water ice opacity, *J. Geophys. Res.*, *114*, E10006, doi: 10.1029/2009JE003358.

Kuroda, T., N. Hashimoto, D. Sakai, and M. Takahashi (2005), Simulation of the Martian Atmosphere Using a CCSR/NIES AGCM, *J. Met. Soc. Japan*, *83* (1), 1-19.

Kuroda, T., A.S. Medevedev, P. Hartogh, and M. Takahashi (2009), On Forcing the Winter Polar Warmings in the Martian Middle Atmosphere during Dust Storms, *J. Meteor. Soc. Japan*, *87*(5), 913-921.

Lee, C., W.G. Lawson, M.I. Richardson, N.G. Heavens, A. Kleinböhl, D. Banfield, D.J. McCleese, R. Zurek, D. Kass, J.T. Schofield, C.B. Leovy, F.W. Taylor, A.D. Toigo, (2009), Thermal tides in the Martian middle atmosphere as seen by the Mars Climate Sounder, *J. Geophys. Res.*, *114*, E03005, doi:10.1029/2008JE003285.

Lewis, S.R., P.L. Read, B.J. Conrath, J.C. Pearl, and M.D. Smith (2007), Assimilation of thermal emission spectrometer atmospheric data during the Mars Global Surveyor aerobraking period, *Icarus*, *192*(2), 327-347.

Lindzen, R.S. and A.Y. Hou (1988), Hadley circulations for zonally averaged heating centered off the equator. *J. Atmos. Sci.*, *45*, 2416-2427.

McCleese, D. J., J. T. Schofield, F. W. Taylor, S. B. Calcutt, M. C. Foote, D. M. Kass, C. B. Leovy, D. A. Paige, P. L. Read, and R. W. Zurek (2007), Mars Climate Sounder: An investigation of thermal and water vapor structure, dust and condensate distributions in the atmosphere, and energy balance of the polar regions, *J. Geophys. Res.*, *112*, E05S06, doi:10.1029/2006JE002790.

Moudden, Y., and J. C. McConnell (2005), A new model for multiscale modeling of the Martian atmosphere, GM3, *J. Geophys. Res.*, *110*, E04001, doi:10.1029/2004JE002354.

Murphy, J. R., R. M. Haberle, O. B. Toon, and J. B. Pollack (1993), Martian Global Dust Storms: Zonally Symmetric Numerical Simulations Including Size-Dependent Particle Transport, *J. Geophys. Res.*, *98*(E2), 3197–3220.

Richardson, M.I. and R.J. Wilson (2002), A topographically forced asymmetry in the martian circulation and climate. Nature *416* (6878), 298-301.

Richardson, M. I., R. J. Wilson, and A. V. Rodin (2002), Water ice clouds in the Martian atmosphere: General circulation model experiments with a simple cloud scheme, *J. Geophys. Res.*, *107*(E9), 5064, doi:10.1029/2001JE001804.

Richardson, M. I., A. D. Toigo, and C. E. Newman (2007), PlanetWRF: A general purpose, local to global numerical model for planetary atmospheric and climate dynamics, *J. Geophys. Res.*, *112*, E09001, doi:10.1029/2006JE002825.

Schneider, E.K. (1983), Martian great dust storms: interpretive axially symmetric models, *Icarus*, *55*(2), 302-331.

Smith, M. D., J. C. Pearl, B. J. Conrath, and P. R. Christensen (2001), Thermal Emission Spectrometer results: Mars atmospheric thermal structure and aerosol distribution, *J. Geophys. Res.*, *106*, 23,929–23,945, doi:10.1029/2000JE001321.

Sprague, A. L., W. V. Boynton, K. E. Kerry, D. M. Janes, N. J. Kelly, M. K. Crombie, S. M. Nelli, J. R. Murphy, R. C. Reedy, and A. E. Metzger (2007), Mars' atmospheric argon: Tracer for understanding Martian atmospheric circulation and dynamics, *J. Geophys. Res.*, *112*, E03S02, doi:10.1029/2005JE002597.

Takahashi, Y. O., H. Fujiwara, H. Fukunishi, M. Odaka, Y.-Y. Hayashi, and S. Watanabe (2003), Topographically induced north-south asymmetry of the meridional circulation in the Martian atmosphere, *J. Geophys. Res.*, *108*(E3), 5018, doi:10.1029/2001JE001638.

Wallace, J.M. and P.V. Hobbs (1976), *Atmospheric Science: An Introductory Survey*, 467 pp. Academic Press, New York.

Wilson, R.J. (1997), A general circulation model simulation of the Martian polar warming,. *Geophys. Res. Lett., 24* (2), 123-126.

Wilson, R.J. and K. Hamilton (1996), Comprehensive model simulation of thermal tides in the martian atmosphere, *J. Atmos. Sci.*, *54*, 1290-1326.

Wilson, R. J., D. Banfield, B. J. Conrath, and M. D. Smith (2002), Traveling waves in the Northern Hemisphere of Mars, *Geophys. Res. Lett.*, *29*(14), 1684, doi:10.1029/2002GL014866.

Wilson, R. J., S. R. Lewis, L. Montabone, and M. D. Smith (2008), Influence of water ice clouds on Martian tropical atmospheric temperatures, *Geophys. Res. Lett.*, *35*, L07202, doi:10.1029/2007GL032405.

Zalucha, A. M., R. A. Plumb, and R. J. Wilson (2010), An Analysis of the Effect of Topography on the Martian Hadley Cells, *J. Atmos. Sci.*, in press, doi: 10.1175/2009JAS3130.1.

Zurek, R. W., and S. E. Smrekar (2007), An overview of the Mars Reconnaissance Orbiter (MRO) science mission, *J. Geophys. Res.*, *112*, E05S01, doi:10.1029/2006JE002701.

Zurek, R.W., J.R. Barnes, R.M. Haberle, J.B. Pollack, J.E. Tillman, and C.B. Leovy (1992), Dynamics of the Atmosphere of Mars in H.H. Kieffer, B.M. Jakosky, C.W. Snyder, and M.S. Matthews, *Mars*, 1498 pp., University of Arizona Press, Tucson.